DOI: 10.1007/s40684-014-0039-7

Design Principles of Co-Planar Interdigitated Micro-Electrode Arrays for Solid-State Ionic Devices

Hyoungchul Kim[1,#] and Hue-Sup Song[2]

1 High-Temperature Energy Materials Research Center, Korea Institute of Science and Technology, Hwarangno 14-gil 5, Seongbuk-gu, Seoul, South Korea, 136-791
2 Division of Advanced Materials Engineering, Kongju National University, Cheonan-daero 1223-24, Cheonan, Chungnam, South Korea, 331-717
Corresponding Author / E-mail: hyoungchul@kist.re.kr, TEL: +82-2-958-5519, FAX: +82-2-958-5529

KEYWORDS: Interdigitated microelectrode, Ion transport, Electrode design, Fuel cells, Finite element method

Comprehensive analyses on the complex ion transport of co-planar interdigitated microelectrode arrays in solid-state ionic devices were carried out using finite element and analytical methods. We found that the ion flux between anode and cathode was constricted on the edges of both electrodes. Based on these results, we defined/analyzed the effective length and ohmic area-specific-resistance of various cell configurations (i.e., electrode width and electrolyte thickness). Using the relation between the effective length and the ohmic area-specific-resistance, we found an analytical model having favorable agreement with the finite element results and propose design rules for high-performance and densely integrated devices.

Manuscript received: July 21, 2014 / Revised: September 4, 2014 / Accepted: September 5, 2014

NOMENCLATURE

ASR_{ohmic} = ohmic area-specific-resistance
d = electrode spacing
i_x = local current density at point x
I = cumulative current density
IMA = interdigitated micro-electrode array
MEA = membrane-electrode assembly
SAT_x = saturation factor of x
t = electrolyte thickness
w = electrode width
x_{eff} = effective length
x_0 = full length of configuration factor x
σ_{ion} = ionic conductivity
ϕ = spatially-varying potential

1. Introduction

The characteristics of many electrochemical energy devices (e.g., fuel cells, solar cells, and batteries) strongly depend on various carrier transport phenomena in the membrane-electrode assembly (MEA).[1-4] As the demands for high-performance and densely integrated energy devices increase, ion transport through an MEA with co-planar interdigitated microelectrode arrays (IMAs) has been considered one of the most important cell configurations.[1,5-7] Recent IMA studies[6,8-19] have reported that its ionic transport characteristics and irreversibility are affected by electrode configuration, multiple interfaces, and nano-scale material effects. Fleig et al.[10] pointed out that the simple size reduction of conventional devices does not fulfill the requirements for small-size portable applications. According to their results, the anomalous current constraints result from the size reduction of cell components and the area-specific cell resistance depends on the electrochemical electrode resistance and the stripe width for various stripe distances and electrolyte thicknesses. Hertz and Tuller[18] also reported that the co-planar IMAs on the electrolyte surface exhibit additional electrolytic resistance due to current constriction near the triple phase boundaries. They reported that constriction resistance dominates the total resistance of a thick electrolyte sample but is relatively small for a thin-electrolyte device. Recently, Kim et al.[19] reported significant potential loss in integrated microelectrode cells. They proposed various alternative designs for the suppression of ion leakage (e.g., electrolyte isolation and electrode compartment). However, so far due to the absence of any quantitative analyses on the ion transport of IMAs, fundamental understanding of ion transport characteristics and reliable prediction of cell ohmic loss with respect to all configuration factors have not been achieved.

In this study, we carried out comprehensive analyses on the anomalous ion transport of co-planar IMAs using the finite element and analytical methods. We investigated the potential and ion flux distribution, and defined the effective lengths of electrode and electrolyte with respect to various configuration factors. Combining these results, we derived an analytic expression to predict the cell ohmic resistance, and we propose design rules useful for finding the optimal MEA configurations.

2. Model Formulation

Fig. 1(a) shows an MEA containing the co-planar configuration of IMAs on a flat electrolyte, a computational domain in this study. Using three independent configuration factors [electrode width ($2w$), electrolyte thickness (t), and electrode spacing (d)], we solve the governing equation regarding the charge conservation of ion, Poisson's equation:

$$-\nabla \cdot \sigma_{\text{ion}} \nabla \varphi = 0 \tag{1}$$

where ϕ is the spatially-varying potential, and σ_{ion} is the ion conductivity. Here, we choose 8 mol% yttria-stabilized zirconia (YSZ) as an electrolyte material because it is a one of the most popular pure oxygen ion conductors. We use the available experimental result for $\sigma_{\text{ion,YSZ}}$; the ionic conductivity of bulk YSZ is 0.13 S/cm at 1000°C.[20] In Fig. 1(b), the governing equation and boundary conditions used for these calculations are shown. The specific potential (ϕ_o) from 0 to –0.9 V is applied to the interface of anode and electrolyte. Compared to that, the potential of 0 V is set to the interface between cathode and electrolyte. The other boundaries are defined as an electric insulation (i.e., zero current) and a symmetry condition. All simulations are performed with a commercial software package (Comsol Multiphysics 3.4: Comsol AB, Sweden), which utilizes the finite element method (FEM) to solve differential equations over a given geometry.

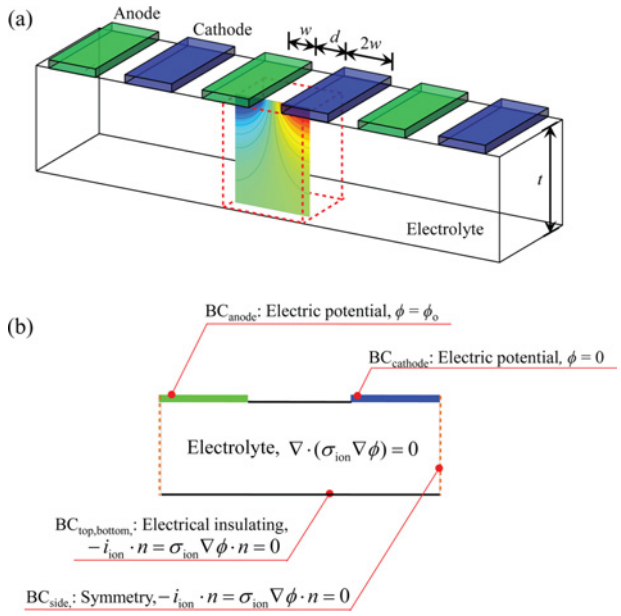

Fig. 1 (a) Three-dimensional cell configuration with co-planar IMAs. The computational variables are also shown. (b) Schematic illustration of computational domain, governing equations, and boundary conditions

To simplify this model simulation, we use the following four assumptions: (i) both electrodes (i.e., anode and cathode) are well-established with a mixed ionic-electronic conductor which has a highly porous microstructure and enough electrochemical catalytic activity; (ii) the electrochemical reactions uniformly take place over the entire interface between the electrode and electrolyte; (iii) each electrode is considered as an ideal ionic source and sink, and any polarization loss of each electrode is not applied; (iv) other unusual ion transport mechanisms (e.g., surface migration and interfacial conduction) are not considered here.

3. Results and Discussion

3.1 Definition of Effective Length

As described in previous paragraph, the potential and current density distributions for an MEA structure are computed for various IMA configurations. Using these results, we show the dimensionless current distributions for each structure [Figs. 2(a) to (d)]. This dimensionless value, normalized cumulative current density defined by

$$\frac{I_x}{I_{x_0}} = \frac{\int_0^x i(x)dx}{\int_0^{x_0} i(x)dx}, \tag{2}$$

where $i(x)$ is the local current density at point x, I_x is the cumulative current density from 0 to x, and x_0 is the full length of configuration factor x, are presented as a function of the normalized distance (i.e., the distance proportion to full configuration length, x/x_0).

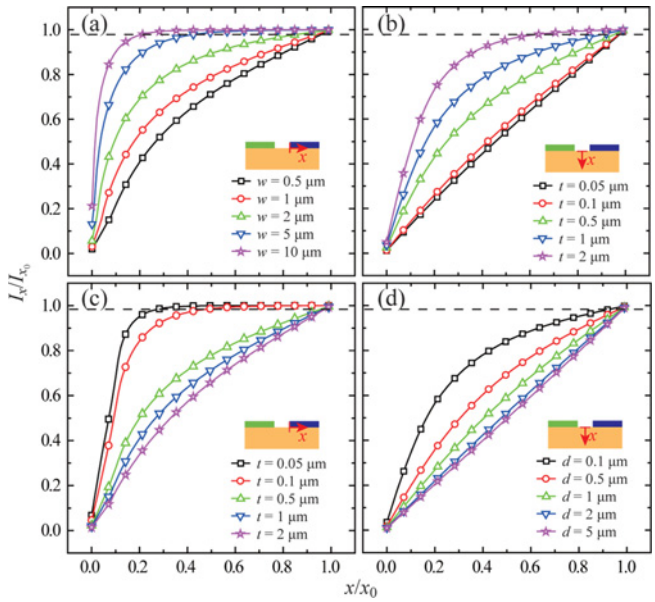

Fig. 2 Variations of the normalized cumulative current density using normalized distance. Fixed configurations [d = 0.1 and t = 1 μm for (a); $2w$ = 1 and d = 0.1 μm for (b); $2w$ = 1 and d = 0.1 μm for (c); $2w$ = 1 and t = 1 μm for (d)] are used. The red arrow in inset shows the starting point and direction for calculating the cumulative current density

These plots along the lateral (or vertical) transmission line of various models show several distinct features in relation to unusual current constriction. The normalized current densities of a few limited

configurations (i.e., small w and t) follow a linear relation, while the other curves (i.e., large w and t) reach a plateau. For example, the tangential slope in Fig. 2(a) converges to zero early as w increases but becomes constant as w decreases. In Fig. 2(b), the cumulative current densities for electrolyte also reach a plateau early for large t. This means that most ions flow near the top surface of the thick electrolyte. Based on these results, we find the configuration factors of co-planar IMAs result in significant current constrictions on the edge (or top) region of an electrode (or electrolyte). Such unusual behavior has also been observed and verified in other model studies [Figs. 2(c) and (d)].

To quantify such current constriction phenomena, we employ the effective length (x_{eff}) of electrode (or electrolyte) defined by

$$I_{x_{\text{eff}}} = \int_0^{x_{\text{eff}}} i(x)dx = 0.99 \int_0^{x_0} i(x)dx = 0.99 I_{x_0} . \quad (3)$$

The effective electrode width (or electrolyte thickness) is defined as the distance from the near- to the opposite-side electrode (or from the top- to bottom-side of electrolyte) where the cumulative current density equals 99% of the total current density. We confirm that this conceptual definition is definitely valid and useful to describe the distinct current constrictions of the co-planar IMAs in Fig. 2. By applying Eq. (3) to Figs. 2(c) and (d), for example, we find the effective electrode and electrolyte lengths as follows: (i) the effective electrode widths (w_{eff}) for $t = 0.05$ and 0.1 μm are 0.154 ($w_{\text{eff}}/w = 0.308$) and 0.268 μm ($w_{\text{eff}}/w = 0.535$), respectively; (ii) the effective electrolyte depths (t_{eff}) for $d = 0.1$ and 0.5 μm are 0.959 ($t_{\text{eff}}/t = 0.959$) and 0.980 μm ($t_{\text{eff}}/t = 0.980$), respectively.

3.2 Prediction of Effective Length Using Saturation Factor

To predict the effective length for any configured MEA model, a series of numerical simulations with the variation of three configuration factors ($2w$, d, and t) are performed. Starting with the effective electrode and electrolyte lengths in each configuration from Eq. (3), the saturation factor (SAT_x) is defined as the ratio of effective length (x_{eff}) to the full length (x_o) for any specific configuration x:

$$SAT_x = x_{\text{eff}}/x_0 . \quad (4)$$

As shown in Fig. 3, this dimensionless parameter provides convenience for visualizing the relative intensity of current constriction in any MEA configuration.

Fig. 3(a) shows the contour plots of SAT_w, and they show the quantitative information for predicting the effective electrode width. With the fixed electrode spacing ($d = 1$ μm) and electrolyte thickness ($t = 0.1$ μm), for example, the SAT_w values of $2w = 10$ μm (i.e., $2w/t = 100$) and 0.1 μm (i.e., $2w/t = 1$) are 0.049 and 0.982, respectively. That is, only 4.9% of the electrode width is utilized for the total electrode width of $2w = 10$ μm, while 98.2% is the effective width for that of $2w = 1$ μm. Interestingly these two-dimensional SAT_w patterns obtained from the fixed d conditions are highly independent of the other configuration factors (w and t) [Fig. 3(a)]. All contour plots share a similar two-dimensional contour pattern for any specific d value. In detail, the SAT_w value for $2w/t << 10$ is fully saturated (red zone; i.e., the weak current constriction), while that for $2w/t >> 10$ is highly constricted (blue zone; i.e., the severe current constriction).

Similarly, the contour plots of SAT_t for four electrode widths ($2w$ = 0.1, 1, 10, and 100 μm) are shown in Fig. 3(b). From the SAT_t values described here, we can find the effective thickness of an electrolyte easily. With fixed configuration factors ($t = 10$ μm and $d = 1$ μm), for example, the SAT_t values for $2w$ = 1 and 100 m are predicted as 0.296 and 0.975, respectively. The effective electrolyte depths are finally obtained as 2.96 and 9.75 μm, respectively. Compared with the effective width, we note that effective electrolyte depth is highly dependent on all configuration factors (d, t, and $2w$). As shown in Fig. 3(b), the red zone, a highly saturated region ($SAT_t > 0.90$), extends toward the right when the $2w$ value increases. Especially for the $2w > 100$ μm, most SAT_t values exceed 0.90 due to their strong dependency on $2w$ [see Fig. 3(b)].

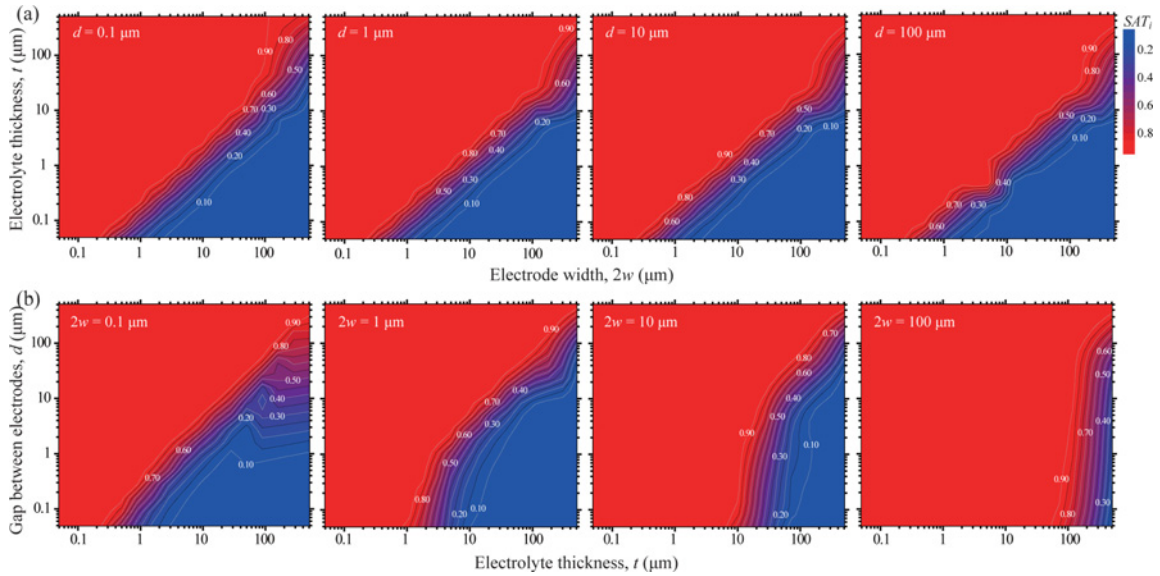

Fig. 3 Contour plots of the saturation factor for various cell configuration factors. The saturation factors of (a) electrode width (SAT_w) and (b) electrolyte thickness (SAT_t) are shown for four different values

3.3 Evaluation of Ohmic Loss for Optimal MEA Layout

Although the effective length is useful to determine the current constriction in the MEA with co-planar IMAs, we know it has many limitations for predicting cell performance and optimizing MEA configurations because it is an indirect indicator from a cell performance perspective. To obtain/predict any direct indicator for evaluating the cell performance (e.g., ohmic area-specific-resistance ASR_{ohmic}) of co-planar IMAs, unfortunately, many numerical simulations (e.g., FEM) are required. If the direct FEM results are not available, the limited analytic method (AM) is an alternative, although these

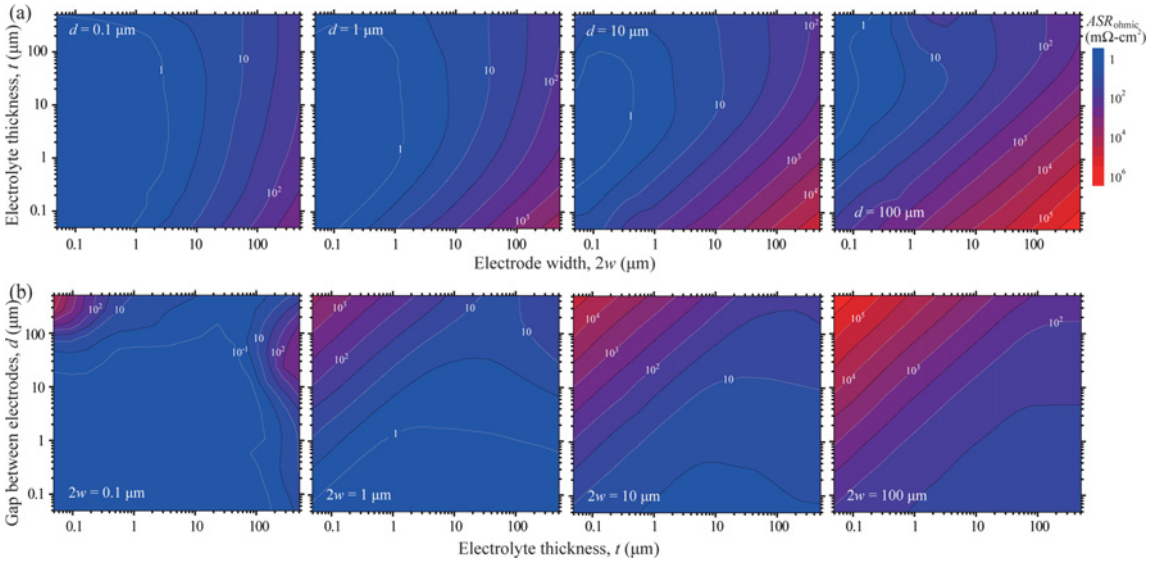

Fig. 4 Contour plots of the ohmic area-specific-resistance for various MEA configurations. The ASR_{ohmic} of (a) four fixed d and (b) $2w$ values are shown

Table 1 Comparison of various ASR_{ohmic} values from finite elements and analytic methods

Geometrical variables (μm)			Effective length (μm)		$ASR_{ohmic,FEM}$	†$ASR_{ohmic,AM}$	‡Ratio
$2w$	t	d	w_{eff}	t_{eff}	(mΩ-cm²)	(mΩ-cm²)	
1	1	1	0.492	0.987	0.858	1.30	1.52
	1	10	0.492	0.990	4.50	4.60	1.02
	1	100	0.492	0.990	42.3	39.0	0.922
	10	1	0.492	2.96	0.829	1.05	1.27
	10	10	0.493	9.75	1.82	1.17	0.643
	10	100	0.494	9.90	6.65	4.60	0.692
	100	1	0.494	2.76	0.980	1.06	1.08
	100	10	0.495	16.9	2.37	1.01	0.426
	100	100	0.495	97.2	7.51	1.16	0.154
10	1	1	2.63	0.988	7.52	8.44	1.12
	1	10	2.60	0.990	43.9	24.7	0.563
	1	100	2.65	0.990	422	210	0.500
	10	1	4.89	9.48	3.88	13.6	3.51
	10	10	4.92	9.86	8.76	13.0	1.48
	10	100	4.92	9.90	46.0	46.0	1.00
	100	1	4.91	13.7	4.42	13.6	3.08
	100	10	4.93	29.5	8.95	10.5	1.17
	100	100	4.94	97.6	20.0	11.7	0.585
100	1	1	2.26	0.988	77.9	7.13	0.0915
	1	10	2.41	0.990	468	22.9	0.0489
	1	100	2.55	0.990	4570	202	0.0442
	10	1	23.9	9.75	32.4	84.0	2.59
	10	10	25.7	9.88	74.9	82.4	1.10
	10	100	26.4	9.90	441	251	0.569
	100	1	48.4	89.8	22.7	184	8.11
	100	10	48.8	94.9	38.2	136	3.65
	100	100	48.6	98.6	86.7	129	1.49

† These results were calculated from Eq. (5)

‡ This is the ratio of $ASR_{ohmic,AM}$ to $ASR_{ohmic,FEM}$

expressions are not in good agreement with experimental results. Here, we derive a new and reliable analytic expression of ASR_{ohmic} with MEA configuration factors including various effective lengths.

To derive the new analytical expression of ASR_{ohmic}, we investigate the exact ASR_{ohmic} of co-planar IMAs obtained from direct FEM simulations. Figs. 4(a) to (b) show the resultant contour plots of ASR_{ohmic} (for different model configurations) obtained from FEMs. Using these two-dimensional maps, we find the exact ASR_{ohmic} for any MEA configuration. For example, the ASR_{ohmic} of 34.9 and 4570 mΩ-cm^2 are obtained for $d = 0.1$ and 100 μm (under $2w = 100$ μm and $t = 1$ μm). In addition, we conclude that the ASR_{ohmic} is generally dependent on all three configuration factors (i.e., proportional to $2w$, d, and $1/t$), while any SAT_x value [e.g., SAT_w in Fig. 3(a)] is quite independent of its configuration factor. Starting from these findings, we derive the analytical expression of ASR_{ohmic} as

$$ASR_{ohmic} = ASR_{ohmic,lat} + ASR_{ohmic,vert}$$
$$= \left(\frac{w_{eff}}{\sigma_{ion}}\right) \cdot \left\{ \left(\frac{d+2t_{eff}}{t_{eff}}\right) + \left(\frac{2}{\pi}\right) \ln\left(\frac{d+2w_{eff}}{d}\right) \right\}, \quad (5)$$

where the subscript lat and vert refer to the lateral and vertical components. The total ASR_{ohmic} can be decomposed as the sum of lateral and vertical parts. They are initiated from the definition of x_{eff}, a combination of the concentric semi-circular (vertical) and straight current line (lateral part), as given in the literature.[21] Table 1 lists the quantitative results from several model configurations and compares these values for two different routes, FEM and AM. The $ASR_{ohmic,AM}$ results obtained from Eq. (5) are in favorable agreement with the aforementioned FEM results, $ASR_{ohmic,FEM}$.

Note that the relation between SAT_x and ASR_{ohmic} is complementary, especially in the MEA optimization with co-planar IMAs pursuing both high-performance operation and densely integrated design. In general, SAT_x values can be useful in evaluating the current constriction, whereas the ASR_{ohmic} is the typical quantity for predicting cell performance. However, we should remember that the SAT_x value has another meaning in the design of an optimized MEA. To design high performance cells with co-planar IMAs, considering ASR_{ohmic} is enough to find optimized MEA configurations with low ohmic resistance. For optimized MEA configurations with densely integrated layout, however, we should consider not only the ASR_{ohmic} but also the SAT_x. Here the SAT_x value provides information about the current constriction and the effective area for electrode and electrolyte, not available in the ASR_{ohmic} results. Such an MEA design strategy is becoming more important with the recent development of micro- and nano-scale energy devices with co-planar IMAs. We believe this design rule based on SAT_x and ASR_{ohmic} offers insights for optimal MEA configurations achieving high-performance and densely integrated devices.

4. Conclusions

Analyzing and optimizing MEA configurations with co-planar IMAs have been challenging in spite of increased demand for their application in high-performance and densely integrated devices. Here, we presented comprehensive analyses on ion transport through the MEA with co-planar IMAs using the finite element and analytical methods. To analyze its unusual current constriction, we defined and used the effective lengths for electrode width and electrolyte thickness with respect to three configuration variables ($2w$, d, and t). The ASR_{ohmic} results were also investigated by the exact FEM and a newly suggested analytic equation. This provided reasonable results for evaluating current constriction and optimizing MEA configurations. For minimal ohmic loss and efficient integration of the MEA with co-planar IMAs, we proposed new design rules consisting of the effective length and ohmic loss (smallest SAT_w, largest SAT_t, and smallest ASR_{ohmic}). In future, we hope to expand these methods and design rules to low-temperature operation (below 600^{o}C), at which electrode polarization becomes more significant, considering the electrode resistance. We believe these design rules for the MEA with co-planar IMAs can lead to promising technological advances in the development of advanced solid-state ionic devices.

ACKNOWLEDGEMENT

This research was financially supported by the institutional research program of the Korea Institute of Science and Technology (2E24691) and the Global Frontier R&D Program on Center for Multiscale Energy Systems (2011-0031579) funded by the National Research Foundation under the Ministry of Science, ICT & Future Planning, Korea.

REFERENCES

1. Steele, B. C. and Heinzel, A., "Materials for Fuel-Cell Technologies," Nature, Vol. 414, No. 6861, pp. 345-352, 2001.
2. Choi, H., Cho, G. Y., and Cha, S.-W., "Fabrication and Characterization of Anode Supported YSZ/GDC Bilayer Electrolyte SOFC using Dry Press Process," Int. J. Precis. Eng. Manuf.-Green Tech., Vol. 1, No. 2, pp. 95-99, 2014.
3. Hwang, Y.-S., Choi, H., Cho, G. Y., Lee, Y. H., and Cha, S.-W., "Effect of Compression Thickness on Performance of Gas Diffusion Layer of Direct Methanol Fuel Cells," Int. J. Precis. Eng. Manuf.-Green Tech., Vol. 1, No. 3, pp. 215-221, 2014.
4. Lee, W. and Prinz, F. B., "Localized Charge Transfer Reactions near the Pt-Ysz Interfaces using Kelvin Probe Microscopy," Int. J. Precis. Eng. Manuf.-Green Tech., Vol. 1, No. 3, pp. 201-205, 2014.
5. Goodenough, J. B., "Oxide-Ion Electrolytes," Annual Review of Materials Research, Vol. 33, No. 1, pp. 91-128, 2003.
6. Larminie, J., Dicks, A., and McDonald, M. S., "Fuel Cell Systems Explained," Wiley New York, 2nd Ed., pp. 67-226, 2003.
7. Martin, M., "Electrotransport and Demixing in Oxides," Solid State Ionics, Vol. 136-137, pp. 331-337, 2000.
8. Hibino, T., Hashimoto, A., Suzuki, M., and Sano, M., "Proton Conduction at the Surface of Y-Doped BaCeO3," Journal of Physical Chemistry B, Vol. 105, No. 46, pp. 11399-11401, 2001.

9. Jiang, S., "Cell Configurations for performance Evaluation in Planar Solid Oxide Fuel Cells," Journal of Applied Electrochemistry, Vol. 34, No. 10, pp. 1045-1055, 2004.

10. Fleig, J., Tuller, H., and Maier, J., "Electrodes and Electrolytes in Micro-SOFCs: A Discussion of Geometrical Constraints," Solid State Ionics, Vol. 174, No. 1, pp. 261-270, 2004.

11. Lai, T. S. and Barnett, S. A., "Effect of Cathode Sheet Resistance on Segmented-in-Series SOFC Power Density," Journal of Power Sources, Vol. 164, No. 2, pp. 742-745, 2007.

12. O'Hayre, R., Barnett, D. M., and Prinz, F. B., "The Triple Phase Boundary a Mathematical Model and Experimental Investigations for Fuel Cells," Journal of the Electrochemical Society, Vol. 152, No. 2, pp. A439-A444, 2005.

13. Cha, S. W., O'Hayre, R., and Prinz, F. B., "The Influence of Size Scale on the Performance of Fuel Cells," Solid State Ionics, Vol. 175, pp. 789-795, 2004.

14. Sata, N., Eberman, K., Eberl, K., and Maier, J., "Mesoscopic Fast Ion Conduction in Nanometer-Scale Planar Heterostructures," Nature, Vol. 408, pp. 946-949, 2000.

15. Hibino, T., Hashimoto, A., Inoue, T., Tokuno, J.-I., Yoshida, S.-I., and Sano, M., "A Low-Operating-Temperature Solid Oxide Fuel Cell in Hydrocarbon-Air Mixtures," Science, Vol. 288, No. 5473, pp. 2031-2033, 2000.

16. Hibino, T., Tsunekawa, H., Tanimoto, S., and Sano, M., "Improvement of a Single-Chamber Solid-Oxide Fuel Cell and Evaluation of New Cell Designs," Journal of the Electrochemical Society, Vol. 147, No. 4, pp. 1338-1343, 2000.

17. Hibino, T., Hashimoto, A., Yano, M., Suzuki, M., Yoshida, S.-I., and Sano, M., "High Performance Anodes for SOFCs Operating in Methane-Air Mixture at Reduced Temperatures," Journal of the Electrochemical Society, Vol. 149, No. 2, pp. A133-A136, 2002.

18. Hertz, J. L. and Tuller, H. L., "Measurement and Finite Element Modeling of Triple Phase Boundary-Related Current Constriction in YSZ," Solid State Ionics, Vol. 178, No. 13, pp. 915-923, 2007.

19. Kim, H., Kim, S. M., Kim, J., Lee, H.-W., and Lee, J.-H., "Experimental and Computational Analyses of Ionic Current Leakage on the Co-Planar Interdigitated Fuel Cells," Solid State Ionics, Vol. 180, pp. 1534-1538, 2009.

20. Sakai, N., Yamaji, K., Horita, T., Xiong, Y. P., and Yokokawa, H., "Handbook on the Physics and Chemistry of Rare Earths," Elsevier, San Diego, CA, 2005.

21. Aoki, K., "Approximate Models of Interdigitated Array Electrodes for Evaluating Steady-State Currents," Journal of Electroanalytical Chemistry and Interfacial Electrochemistry, Vol. 284, No. 1, pp. 35-42, 1990.